PHYSICAL REVIEW B **76**, 045118 (2007)

Ultrahigh Purcell factor in photonic crystal slab microcavities

Lorenzo Sanchis,* Martin J. Cryan, Jose Pozo, Ian J. Craddock, and John G. Rarity
Center for Communications Research, Department of Electronic and Electrical Engineering, University of Bristol, Bristol BS8 1UB, United Kingdom

(Received 2 February 2007; revised manuscript received 18 April 2007; published 30 July 2007)

The design of high Purcell factor optical photonic crystal slab microcavities by means of two techniques is presented. First, a combination of stochastic optimization algorithms is used to modify the position of the holes made in a dielectric membrane, breaking their periodic pattern. The combined algorithm is a mixture of a genetic algorithm and a simulated annealing algorithm that is shown to work better than if they were used separately. Secondly, the combined algorithm is used to transform a periodic microcavity where subwavelength sized high-index elements have been inserted. Although the optimization is performed over two dimensional structures with the help of the multiple scattering theory, we show that the optimized microcavities maintain their peculiarities when transformed to their three dimensional equivalent slab microcavities using the finite integration technique. We numerically prove the existence of modified microcavities with extremely small mode volumes of 0.086 91 in $(\lambda/n)^3$ units and ultrahigh Purcell factor of 75 with an enhancement factor of 5.36 with respect to the unperturbed microcavity.

DOI: 10.1103/PhysRevB.76.045118 PACS number(s): 42.70.Qs, 42.82.Et, 42.50.Ct

I. INTRODUCTION

Photonic crystal (PC) microcavities with high quality factor (Q) and small mode volumes (V) have many important scientific and engineering applications such as high-resolution sensors,[1] low-threshold nanolasers,[2] ultrasmall filters,[3] and efficient single photon sources.[4] The generation of single photons is crucial for practical implementation of quantum cryptography and quantum key distribution[5] as well as linear optics quantum computation.[6] In the future, microcavities containing single emitters may also be used for nonlinear logic gates in quantum information processing.[7–9]

Since three dimensional (3D) photonic crystals employing distributed Bragg reflection confinement in 3D have not been perfected yet, two dimensional (2D) photonic crystal slabs[10,11] have been proposed as good candidates to support such microcavities. 2D PC microcavities fabricated in a membrane offer many of the benefits of 3D structures with several additional advantages. Due to the easier manufacture by means of present microfabrication and planar techniques, a wide variety of passive and active optical microcavities can be fabricated introducing point or line defects into a periodic array of holes perforating an optically thin semiconductor slab. In these structures, the 2D PC lattice provides in-plane optical confinement, while index guiding is used to achieve confinement in the vertical direction.

The use of 2D PC-slab microcavities enables very large Q factors with small effective mode volumes, approaching the theoretical diffraction limit that corresponds to a cubic half wavelength in the material.[12,13] As we will see later, the other important advantage of these structures is the possibility of using much faster 2D modeling tools to describe and design them.

The Purcell factor (F_P) of a resonant cavity is a measure of the spontaneous emission rate enhancement of a source placed in the cavity with respect to that in the bulk semiconductor. This enhancement leads to an increase in the degree of light-matter interaction for processes such as nonlinear optical responses or coherent electron-photon interactions. The spontaneous emission rate enhancement is useful for efficient pure state single photon sources. The lifetime can be reduced to the point where the photon is effectively time-bandwidth limited, an essential requirement for quantum logic applications.[14]

Under some conditions,[15] F_P can be written as

$$F_P = \frac{3Q(\lambda/n)^3}{4\pi^2 V}, \tag{1}$$

where Q is the quality factor, n is the refractive index at the location of the maximum squared electric field ($\vec{r}_{max}$), and λ is the resonant free space wavelength of the cavity. V is the effective volume of the electromagnetic energy of the resonant mode defined as the ratio of the total electric field energy to the peak value of the electric field energy density:

$$V = \frac{\displaystyle\int \varepsilon(\vec{r})|\vec{E}(\vec{r})|^2 d^3 r}{\varepsilon(\vec{r}_{\max})|\vec{E}(\vec{r}_{\max})|^2}. \tag{2}$$

From Eq. (1), we see that there are two ways to increase the Purcell factor. The first one is to increase the cavity quality factor Q, and the second one is to decrease the effective mode volume V. Although until now most methods to maximize the Purcell factor in PC microcavities have been performed by modifying the cavity geometry in order to increase Q,[3,12,13,16] little progress has been made in creating mechanism for reducing V. In these publications, different procedures are used to reduce the k components within the light cone avoiding out of plane radiation. In some cases, when the cavity's resonance linewidth is much smaller than the emitter's (for example, with color centers in diamond[17] or rare earth metal doped materials), increasing the cavity Q has no effect on the spontaneous emission. This makes a mode volume reduction necessary instead of trying to find an optimized microcavity with high Q since the Q of the cavity is replaced by the Q_m of the material ($Q_m = \omega_e / \Delta\omega_e$, where $\Delta\omega_e$ is the linewidth of the emitter).[18]

Recently, the problem of reducing V of a microcavity has been treated using low-index dielectric discontinuities with subwavelength dimensions where the high field region is located.[19] The use of dielectric discontinuities has shown the possibility to confine, enhance, and guide light in a low-refractive-index material as the core in opposition to the conventional method of total internal reflection.[20] In a high-index contrast interface, to accomplish the continuity of the normal component of the electric flux density $\vec{D}$, the corresponding electric field component must undergo a large discontinuity with much higher amplitude in the low-index region. This effect, considering Eq. (2), has been used to efficiently reduce the mode volume in a high-index contrast microcavity and achieve high Purcell factors as shown by Eq. (1). In Ref. 19, although high mode volume reduction is achieved, the maximum electric field is situated in the low-index region which is formed by air. However, as the use of single quantum dots as emitters seems to be the most promising option for PC single photon sources,[4] the emitter needs to be placed in the semiconductor region instead of the air region. Thus, it is desirable to have the maximum electric field of the mode in a substrate where the quantum dot can be located such as, for example, GaAs. In any event, this configuration may also be attractive in order to maximize the overlap between an active region and the cavity field while designing a laser cavity or a light-emitting diode.

In this paper, we use two different techniques in order to reduce the mode volume of a 2D periodic PC-slab microcavity and we numerically demonstrate that the mode volume reduction produces an enhancement in the Purcell factor. The first technique consists of an appropriate rearrangement of the scattering elements of a periodic PC-slab microcavity. In this case, the cylindrical holes made in a semiconductor slab are repositioned in order to reduce the mode volume by increasing the maximum squared electric field [see Eq. (2)]. The second technique to reduce the mode volume consists of making a similar rearrangement of the position of the holes but this time introducing high-index scattering elements confined within the host dielectric medium of the microcavity inspired by the procedure introduced in Ref. 19.

The microcavity analyzed in this paper is modified by employing an optimization technique consisting of the simultaneous use of two methods: the genetic algorithm (GA)[21] and the simulated annealing (SA).[22] While the binary-coded GA operates on a population of candidate structures to produce new ones with better performance in an iterative process inspired by Darwinian evolution, SA is an optimization method based on the process of slowly cooling a molten metal in order to obtain a uniform crystalline structure. We demonstrate that such a combination of optimizing procedures gives better performance than the sole use of either of them. Although it has been confirmed that GA optimization is an effective tool in the design of photonic[23] or acoustic[24] devices based on the modification of periodic photonic or acoustic band gap crystals, little work has been focused on improving the optimization approach in order to solve a particular problem. In that direction, we have modified the optimization strategy in comparison with previous works, where the symmetry was broken by removing some scattering elements from their periodic lattice sites[23,24] to accomplish a specific functionality (focusing an incident beam). As we are dealing with cavities, the final goal is to keep the light confined in a region surrounded by the PC. Consequently, it is more efficient to move the scattering elements with respect to their initial periodic locations rather than eliminating them. In addition, we have taken into account symmetry considerations with the purpose of reducing the space search of the optimization process.

In order to apply our GA-SA combined optimization procedure, also called inverse design, the direct problem has to be solved. Therefore, it is necessary to calculate the electromagnetic field of a given configuration in a fast and accurate way since it has to be computed several times until convergence of the optimization process. To do that, we utilize a self-consistent method named two dimensional multiple scattering theory (2D-MST).[25] In essence, the method is based on analytically solving the boundary conditions related to each individual scatter in a basis of cylindrical Bessel's functions. Then, the superposition of the waves scattered from each object is used to express the total scattered wave. Although 2D-MST in conjunction with GA has been successfully applied in the design of devices formed by clusters of identical cylindrical scattering elements,[23] in this paper we employ 2D-MST with clusters formed with a combination of different kinds of scatters with different dielectric properties and radii.

With the aim of saving computing effort, a 2D procedure is used for the optimization. Thus, the microcavities used to solve the direct problem are formed by arrays of infinitely deep holes made in an infinitely thick semiconductor slab. Evidently, this configuration is of no use in practice. To ensure that the real 3D counterparts of the 2D microcavities formed by arrays of holes made in finite-thickness semiconductor slabs maintain the optimized functionality, it is necessary to make full 3D calculations. In that direction, we have studied the optimized and nonoptimized 2D microcavities created on slabs of three different thickness: 180, 270, and 540 nm. We use the 3D finite integration technique (FIT) method from CST Microwave Studio package[31] to analyze the resulting structures. To the author's knowledge, the direct comparison between 2D-optimized and 3D counterpart's behavior is not yet available in the literature.

II. 2D-MST ANALYSIS OF PC MICROCAVITIES

In this section, we briefly describe the fundamentals of 2D-MST which are required to apply the optimization techniques used to modify the 2D equivalent of a 3D-slab microcavity. This method is well established; however, it is useful to review it in order to provide sufficient context for the problem in question. In addition, a decrease of the calculation time required in the optimization procedure is achieved by reducing the computational effort by addressing some new relations between the elements of the scattering matrix. For a detailed description of this technique, the reader is referred to Ref. 25 and references therein.

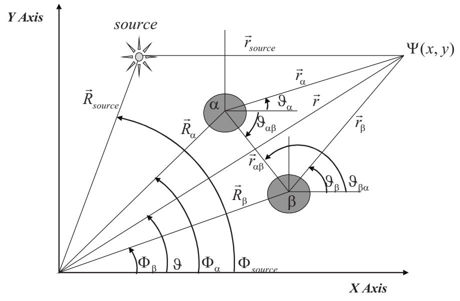

FIG. 1. Coordinate systems and definition of variables employed in the equations of the multiple scattering formalism (see Sec. II).

We want to describe the resonant modes of a microcavity made of an array of infinitely deep cylindrical inclusions in a dielectric medium with their symmetry axis parallel to the z axis in the coordinate system used. The final objective is to calculate the total scattered wave in the XY plane from a discrete number of dielectric scatters (with dielectric constant $\varepsilon_2=1$ for holes) placed in a dielectric background characterized by ε_1 for a polarized fixed incident wave and at a fixed frequency. The scattered wave will be the mode field of the resonant state under proper excitation because the resonant mode is a solution of the Maxwell equations in the absence of any source. The polarization of the incident light is restricted to TE; hence, the magnetic component of the field (the only nonzero one) is parallel to the cylinder's axis. Under this restriction, the full electromagnetic field is completely determined by the z component of the magnetic field $B_z \equiv \Psi$ and the components of the electric field are $E_x = (i/\mu_0\varepsilon_1\omega)(\partial\Psi/\partial y)$ and $E_y = (-i/\mu_0\varepsilon_1\omega)(\partial\Psi/\partial x)$. To deduce these expressions, the Maxwell equation $\nabla\times\vec{B} = \mu_0\varepsilon_1\partial\vec{E}/\partial t$ has been used; we have considered time dependence $e^{-i\omega t}$ and taken into account that $\vec{B}=B(x,y)\vec{u}_z$. It is important to consider that we are dealing with a frequency domain method as opposed to the FIT method. Let us consider an array of N cylinders located at positions $\vec{R}_\beta$ ($\beta=1,2,\ldots,N$) and radius ρ_β. $\vec{R}_\beta$ is a vector in the XY plane that defines the position of cylinder β. The geometry of the problem and the variable definitions are shown in Fig. 1.

If an incident wave Ψ^{inc} comes into contact with the array, the total field around the general cylinder α is a superposition of the incident field and the radiation scattered by the remaining cylinders $\beta\neq\alpha$,

$$\Psi_\alpha = \Psi^{inc} + \sum_{\beta\neq\alpha}^{N} \Psi_\beta^{scatt}, \tag{3}$$

where Ψ_β^{scatt} is the field scattered by the β cylinder. Those fields can be expanded as a combination of Bessel functions centered at the α cylinder position. If the multipole coefficients are $(B_\alpha)_l$, $(S_\alpha)_l$, and $(A_\beta)_l$, for Ψ_α, Ψ_β^{inc}, and Ψ_β^{scatt}, respectively, the expression above can be cast into the following relation between coefficients:

$$(B_\alpha)_l = (S_\alpha)_l + \sum_{\beta=1}^{N}\sum_{l'=-\infty}^{l'=\infty} (G_{\beta\alpha})_{ll'}(A_\beta)_{l'}, \tag{4}$$

$G_{\beta\alpha}$ being the propagator from cylinder β to α whose components are

$$(G_{\beta\alpha})_{ll'} = (1-\delta_{\alpha\beta})e^{i(l'-l)\theta_{\alpha\beta}}H_{l'-l}^{(1)}(k_1 r_{\alpha\beta}), \tag{5}$$

where $\delta_{\alpha\beta}$ is the Kronecker delta ($\delta_{\alpha\beta}=1$ if $\alpha=\beta$, and $\delta_{\alpha\beta}=1$ if $\alpha\neq\beta$), $H_n^{(1)}$ is the outgoing Hankel function of order n and argument $k_1 r_{\alpha\beta}$ which from now on will be denoted simply as H_n, and k_1 is the wave vector in the dielectric medium, $k_1=(\omega/c)\sqrt{\varepsilon_1}$. In this particular case, $n=l'-l$. The propagator allows the field scattered by cylinder β to be expressed in the coordinate system centered on cylinder α and it is deduced using Graf's formula.[26]

Notice that the coefficients $(S_\alpha)_l$ are known because they describe an arbitrary chosen incident field. Our choice was based on the fact that these $(S_\alpha)_l$ coefficients should represent a realistic source. Nevertheless, the coefficients $(B_\alpha)_l$ and $(A_\alpha)_l$ are not known. The boundary conditions of continuity of the field and its derivatives at the surface of the α cylinder relate the coefficients B_α and A_α, thanks to the square and diagonal scattering matrix T_α whose elements $(t_\alpha)_{ll'}$ for TE polarization are

$$(t_\alpha)_{ll'} = \frac{k_2^{-1}J_l(k_1\rho_\alpha)J_l'(k_2\rho_\alpha) - k_1^{-1}J_l'(k_1\rho_\alpha)J_l(k_2\rho_\alpha)}{k_1^{-1}H_l'(k_1\rho_\alpha)J_l(k_2\rho_\alpha) - k_2^{-1}H_l(k_1\rho_\alpha)J_l'(k_2\rho_\alpha)}\delta_{ll'}, \tag{6}$$

where k_1 and k_2 are the wave vector numbers in the dielectric region and in the air region, respectively. Multiplying these coefficients by both sides of Eq. (4) and after some simple algebra, we arrive at

$$(A_\alpha)_l - \sum_{\beta=1}^{N}\sum_{l'=-\infty}^{l'=\infty} (t_\alpha G_{\beta\alpha})_{ll'}(A_\beta)_{l'} = (t_\alpha S_\alpha)_l. \tag{7}$$

By truncating the integers l and l' within $|l|\leqslant l_{\max}$ and $|l'|\leqslant l_{\max}$, Eq. (7) reduces to a linear system of equations of dimension $N(2l_{\max}+1)\times N(2l_{\max}+1)$ that in matrix form reads $MA=S$. In this equation, A and S are column matrices with elements $A_{1l}, A_{2l}, \ldots, A_{Nl}$ and $t_{1l}S_{1l}, t_{2l}S_{2l}, \ldots, t_{Nl}S_{Nl}$, respectively. The matrix M can be considered as the scattering matrix of the whole set of holes and is a square matrix where each element is a submatrix of dimension $(2l_{\max}+1)\times(2l_{\max}+1)$. In short, the matrix elements can be expressed by

$$(M_{\alpha\beta})_{ll'} = \delta_{\alpha\beta}\delta_{ll'} - (t_\alpha G_{\alpha\beta})_{ll'}. \tag{8}$$

As the matrix M has to be calculated several times, the CPU time required in the calculations can be reduced by half using the following relation between the elements of the submatrices $M_{\alpha\beta}$ and $M_{\beta\alpha}$:

$$(M_{\alpha\beta})_{ll'} = \left[(1-\delta_{\alpha\beta})(-1)^{(l'-l)}\frac{(t_\beta)_{ll'}}{(t_\alpha)_{ll'}} + \delta_{\alpha\beta}\right](M_{\beta\alpha})_{ll'}. \tag{9}$$

This relation is obtained from the properties of the polar variables $\theta_{\beta\alpha}-\theta_{\alpha\beta}=\pi$ and $r_{\alpha\beta}=r_{\beta\alpha}$ (see Fig. 1). These properties imply that $(G_{\alpha\beta})_{ll'}=(-1)^{(l'-l)}(G_{\beta\alpha})_{ll'}$, which when introduced into Eq. (8) gives the identity in Eq. (9).

Although the resonant modes studied here are solutions of the system with no source, to obtain the coefficients $(A_\alpha)_l$ it is necessary to properly excite these modes at the resonant frequency. The incident field is determined by the coefficients $(S_\alpha)_l$ which describe the excitation wave on the system of coordinates of cylinder α.

$$\Psi_\alpha^{inc}=\sum_{l=-l_{\max}}^{l=l_{\max}}(S_\alpha)_l J_l(k_1 r_\alpha)e^{il\theta_\alpha}. \tag{10}$$

Let us suppose that we expand the incident field centered at the origin of coordinates as

$$\Psi^{inc}=\sum_{s=-l_{\max}}^{s=l_{\max}}(S_0)_s J_s(k_1 r)e^{ils\theta}. \tag{11}$$

Now, it is necessary to express the coefficients of the excitation field centered at the origin of coordinates $(S_0)_s$ in the system of coordinates of cylinder α. To do so, Graf's formula is used once more.

$$\begin{aligned}\Psi^{inc}&=\sum_{s=-l_{\max}}^{s=l_{\max}}(S_0)_s J_s(k_1 r)e^{ils\theta}\\&=\sum_{s=-l_{\max}}^{s=l_{\max}}(S_0)_s\sum_{l=-l_{\max}}^{l=l_{\max}}e^{i(s-l)\Phi_\alpha}J_{s-l}(k_1R_\alpha)J_l(k_1r_\alpha)e^{il\theta_\alpha}\\&=\sum_{l=-l_{\max}}^{l=l_{\max}}(S_\alpha)_l J_l(k_1 r_\alpha)e^{il\theta_\alpha},\end{aligned} \tag{12}$$

where the coefficients $(S_\alpha)_l$ are

$$(S_\alpha)_l=\sum_{s=-l_{\max}}^{s=l_{\max}}(S_0)_s e^{i(s-l)\Phi_\alpha}J_{s-l}(k_1R_\alpha). \tag{13}$$

In the following, we will use 2D magnetic point sources as excitation elements. Considering TE polarization, a 2D magnetic point source is an oscillating current along the z direction at position $\vec{R}_{source}=(x_{source},y_{source})$ represented by a Hankel function of order zero. $\Psi^{inc}=H_0(k_1|\vec{r}-\vec{R}_{source}|)$ that centered at the origin using Graf's formula is

$$\begin{aligned}\Psi^{inc}&=H_0(k_1|\vec{r}-\vec{R}_{source}|)\\&=\sum_{s=-l_{\max}}^{s=l_{\max}}e^{-is\Phi_{source}}H_{-s}(k_1R_{source})J_s(k_1r)e^{is\theta}.\end{aligned} \tag{14}$$

Comparing Eqs. (14) and (11), we get the coefficients that describe the incident field as a function of the position of the source,

$$(S_0)_s=e^{-is\Phi_{source}}H_{-s}(k_1R_{source}). \tag{15}$$

Finally, the unknown coefficients of the column matrix A can be obtained by matrix inversion. The field of the resonant mode on the dielectric region is the sum of the scattered fields of all the cylinders:

$$\Psi_{mode}(x,y)=\sum_{\alpha=1}^{N}\sum_{l=-l_{\max}}^{l=l_{\max}}(A_\alpha)_l H_l(k_1r_\alpha)e^{il\theta_\alpha}. \tag{16}$$

With the preceding formalism, we are able to determine the mode profile in the high-index region for a given frequency. Notice that an equivalent procedure is possible in order to obtain the field inside the holes. Nevertheless, as it will be shown in Secs. IV and V, for the structure to be studied with the use of the proposed optimization algorithm, it is not necessary to know the field in the low-index regions (holes). For the sake of simplicity and to perform faster calculations, we have set these values equal to zero. Once the 2D-optimized microcavity is obtained, the whole field profile will be calculated in 3D space (holes inclusive) with the FIT method in order to deduce the microcavity Purcell factor which we wish to enhance. Finally, this Purcell factor will be compared with that of a periodic nonoptimized microcavity.

III. UNPERTURBED MICROCAVITY

In this paper, we will start from an unperturbed microcavity using GA-SA optimization to improve its performance. More specifically, we will enhance its Purcell factor by the reduction of the mode volume while, at the same time, maintaining or eventually increasing the value of Q. It is therefore crucial to know the characteristics of the original or unperturbed microcavity to compare with the ones obtained with the optimization strategies that we will use. Also, it is essential to know how these characteristics are transformed when an additional dimension is added; passing from a 2D microcavity to its 3D counterpart, for example, we will see a shift in the resonant frequency. The motivation for this is that while we are finally interested in a 3D structure, the optimization process will be done under 2D constraints. Therefore, our goal is to achieve a relative enhancement of the Purcell factor between the 3D optimized microcavity, the counterpart of the 2D-optimized one, and the 3D unperturbed one. First, the 2D unperturbed microcavity will be studied with the help of MST and FIT, and then, the 3D case will be considered using FIT.

The periodic unperturbed single-defect 2D microcavity treated in this section (see Fig. 2) consists of a missing hole in a hexagonal array of holes ($\varepsilon_2=1$, or $n_2=1$) made in an infinite-thickness slab of GaAs ($\varepsilon_1=12.6$, or $n_1=3.55$). The defect region is surrounded by four layers of holes with lattice constant $a=280$ nm and radius $r=0.33a=92.4$ nm. We want to stress that such reduced number of holes is determined by our computational resources given that, for the optimization process, the mode field must be calculated several times. It is important to remember the fact that we are interested in the relative improvement of the Purcell factor between an unperturbed and a perturbed microcavity to validate our method and promote its use in future work. Therefore, the inclusion of additional holes will not help us in our purpose.

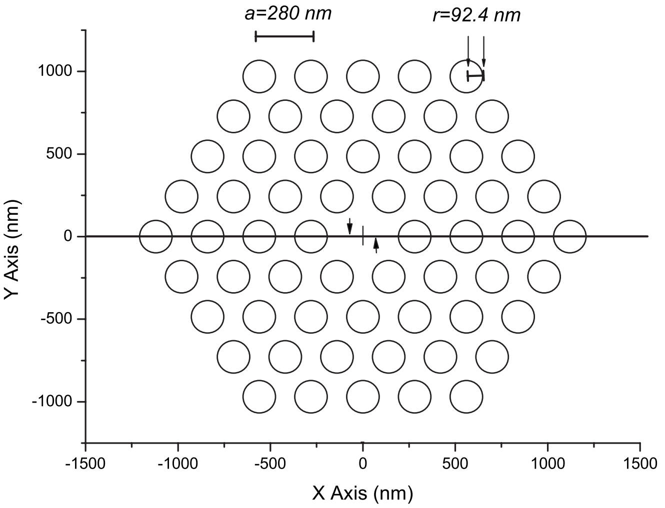

FIG. 2. Unperturbed structure with parameters $a=280$ nm and $r=92.4$ nm considered in Sec. III. The two magnetic monopole sources in opposite phases are represented as small arrows near the center of the cavity. They are located at $x=\pm 94$ nm, $y=0$ nm.

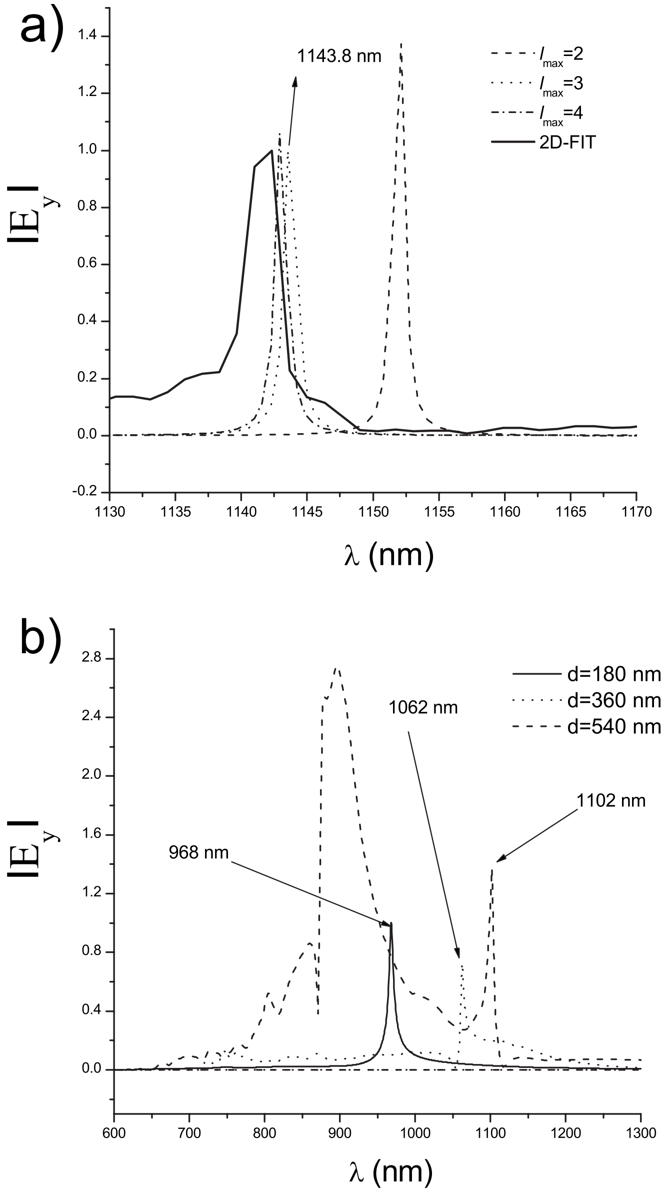

FIG. 3. (a) Multiple scattering (dotted lines) and 2D-FIT (continuous line) calculation of the spectrum of the unperturbed microcavity presented in Fig. 2. Three different values are used for the integer l_{max}. The resonant wavelength used throughout this work, corresponding to $l_{max}=3$, is 1143.8 nm. The peak value of the y component of the electric field for $l_{max}=3$ is normalized for further comparison purposes. (b) Wavelength response of the unperturbed microcavity when a third dimension is added. The calculation of the electric field y component at the middle of the slab is made with full 3D-FIT formalism for three different slab thicknesses $d=180$ nm, $d=360$ nm, and $d=540$ nm. The resonant y-dipole modes have been linked to their resonant wavelength in order to be distinguished from other mode features (see the case $d=540$ nm).

It is well known[13] that the sort of microcavity studied here supports a doubly degenerated dipole mode. Let us focus on the y-dipole mode which, in principle, has maximum y electric field component (the only nonzero one) at the center of the microcavity, in this case, coincident with the center of coordinates. The first step is to find the resonant wavelength of that mode with the MST formalism. We excite the cavity using two magnetic point sources (see Sec. II) in opposite phase located at the points $x=\pm 94$ nm, $y=0$ nm (see small arrows in Fig. 2). These points have been chosen on antinode positions of the magnetic field pattern of the y-dipole resonant field B_z in order to excite the mode efficiently. Note that if, for example, a single source was to be located at the microcavity center, only the monopole mode would be excited. However, here we are interested in modes with high electric field at the geometrical center of the cavity. Figure 3 shows the response of the modulus of the E_y component at the central position between magnetic sources (origin of coordinates) as a function of the exciting wavelength (in air) for different cases. In the preceding section, it has been shown that the integer $l_{\max}$ has to be truncated in order to solve the linear system of equations expressed with Eq. (7). Therefore, the higher $l_{\max}$, the more accurate will be the calculation of the resonant frequency. In order to identify the option that is the best compromise between computation time and accuracy, Fig. 3(a) shows the cavity wavelength response for three different values of $l_{\max}$ in conjunction with the same calculation using 2D-FIT. It can be seen that making $l_{\max}$ higher than 3 does not significantly improve the convergence given by the value calculated with 2D-FIT. The difference between the resonant peak for $l_{\max}=4$ (1143 nm), that has been proved to be converged, and the peak obtained with the 2D-FIT (1142 nm) is slightly different due to grid discretization. This fact reveals the analytical character of the multiple scattering formalism, where the accuracy is determined by the number of terms of the field expansion $(2l_{\max}+1)$ against the numerical character of the FIT where the accuracy is determined by the discretization in space and time. With these results in mind, unless stated, our choice for $l_{\max}$ is 3 which gives a reasonably converged result with resonant wavelength of 1143.8 nm. The peak value of the y electric field component at this wavelength has been normalized because in the following it will be used as a reference with different perturbed microcavities. For the calculations made with 2D-FIT, we place a broad band dipole source in the center of the microcavity oriented along the y axis and we input a short few-cycle excitation pulse to probe the temporal response of the y component of the electric field in that point. The y-dipole mode of the cavity then rings at the resonant frequency, and taking the Fourier transform of the ring-down signal allows us to determine the cavity frequency, response and hence the resonant frequency of the mode. Mesh sizes of 12 nm have been used in the x and y directions in all 2D simulations.

We now focus on a realistic situation in which the thickness of the slab is a finite magnitude. With the use of full 3D-FIT calculation, we show in Fig. 3(b) the response of the same unperturbed microcavity but this time for three different slab thicknesses $d=180$ nm, $d=360$ nm, and $d=540$ nm. Here, nonuniform meshing is used in the vertical direction with a mesh size of 3.75 nm within the slab and 5 nm outside. In the XY plane, we use a mesh size of 3.75 nm in all the calculation space. It has been found that for the 3D-FIT case, the use of an excitation dipole located at the center of the slab causes the appearance of unrealistic field peaks because of reflection from the excitation element. These undesired numerically induced artifacts can lead to unrealistic mode volume estimations. In order to avoid this situation, the excitation of the cavities has been performed from outside by the use of two y-oriented dipoles located in the z axis at a distance of 460 nm from each side of the slab ($z=-460$ nm and $z=d+460$ nm). The y-dipole mode is characterized by sharp peaks at different wavelengths for different slab thicknesses with resonant wavelengths of 968, 1062, and 1102 nm. For the particular case where the slab thickness is 540 nm, additional resonant features are observable at low wavelengths corresponding to modes with different nature from the one we are interested in. The position shift of the resonances with the slab thickness is consistent with the generalized procedure of using a thickness-dependent effective refractive index when in-plane 2D simulations are performed to account for the third dimension. Therefore, the increase in the effective index "seen" by the resonant mode by increasing the slab thickness results in a corresponding enlargement of the "cavity size," and accordingly, the resonant wavelength shifts to longer values. A further increase of the slab thickness beyond $d=540$ shifts the resonant wavelength to the previous results calculated with 2D-MST and 2D-FIT methods.

To calculate the resonant wavelength with the 2D formalism, the effective index concept was not utilized since, in both cases (MST and FIT), the true value for the refractive index of the GaAs, $n_1=3.55$, was used. Consequently, for the case that we have focused on ($l_{\max}=4$ for 2D-MST), the wavelength obtained with the 2D-MST method is redshifted approximately 173, 80, and 40 nm with respect to the value obtained with the 3D-FIT method for the three slab thicknesses $d=180$ nm, $d=360$ nm, and $d=540$ nm, respectively. Although these resonant wavelengths are different, for the scope of this work it is still interesting to know if these modes are in-plane geometrically equivalent. To answer this, we compare the mode profiles along the x axis. In Fig. 4, the y component of the electric field at resonance calculated by different methods is shown. As has been shown previously, the fact that the resonant peaks are in the same position reveals the equivalence between 2D-MST and 2D-FIT. In Fig. 4(a), this equivalence can also be seen but this time observing that the mode profile coincides almost perfectly. It must be remembered that the field inside the holes has been set to zero when the MST calculation is used. However, the FIT formalism is able to determine the field in the entire computational space. Once we have proved such equivalence, it is important to compare the mode profiles for the case of 3D slabs. In Fig. 4(b), we put side by side the mode profiles obtained with 3D-FIT method with slab thicknesses $d=180$ nm, $d=360$ nm, and $d=540$ nm. Although they have been calculated at different resonant wavelengths, their similarity is remarkable since the only difference is the relative height of the side peaks with respect to the central one. We observe in the $d=360$ nm and $d=540$ nm cases that the maximum electric field is located near the internal edges of the holes in contrast to the $d=180$ nm case where the maximum electric field is on the center of the microcavity. It is therefore shown that for the three 3D microcavities, only in the $d=180$ nm case the maximum electric field region is located at the center of the cavity where a source like a quantum dot can be situated. This is convenient if we desire an efficient geometrical coupling between the source and the cavity mode in order to efficiently modify its spontaneous emission rate. Therefore, proving the in-plane geometric mode profile equivalence of the 2D-MST and the 3D-FIT supports, in principle, our proposal of performing the optimization in a 2D structure. Also, although not shown here, it has been shown that in the 3D cases, the polarization of this mode is predominantly TE inside the high-index slab, a fact that corroborates the equivalence between 2D and 3D in this particular kind of microcavities.

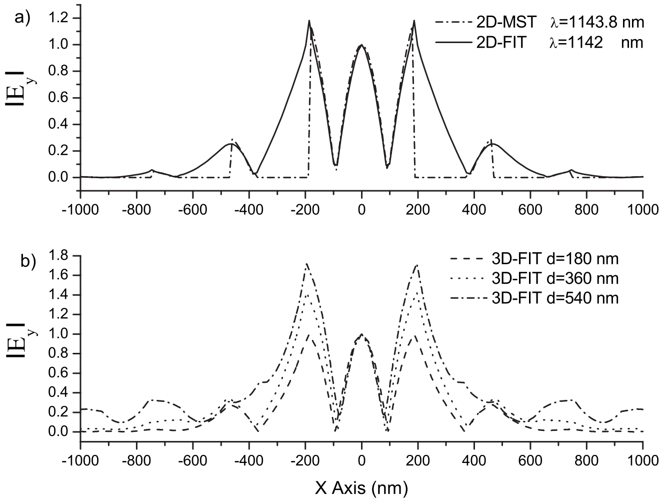

FIG. 4. (a) Normalized mode profile comparison along the x axis of the resonant mode calculated with 2D-MST (dash-dotted line) and 2D-FIT (continuous line) procedures. In the zones where holes are located, the value of the field for the MST case has been set to zero. (b) The same as (a) but this time with the 3D-FIT procedure for the $d=180$ nm, $d=360$ nm, and $d=540$ nm cases. The resonant wavelengths are shifted with respect to the 2D-MST calculation around 173, 80, and 40 nm, respectively.

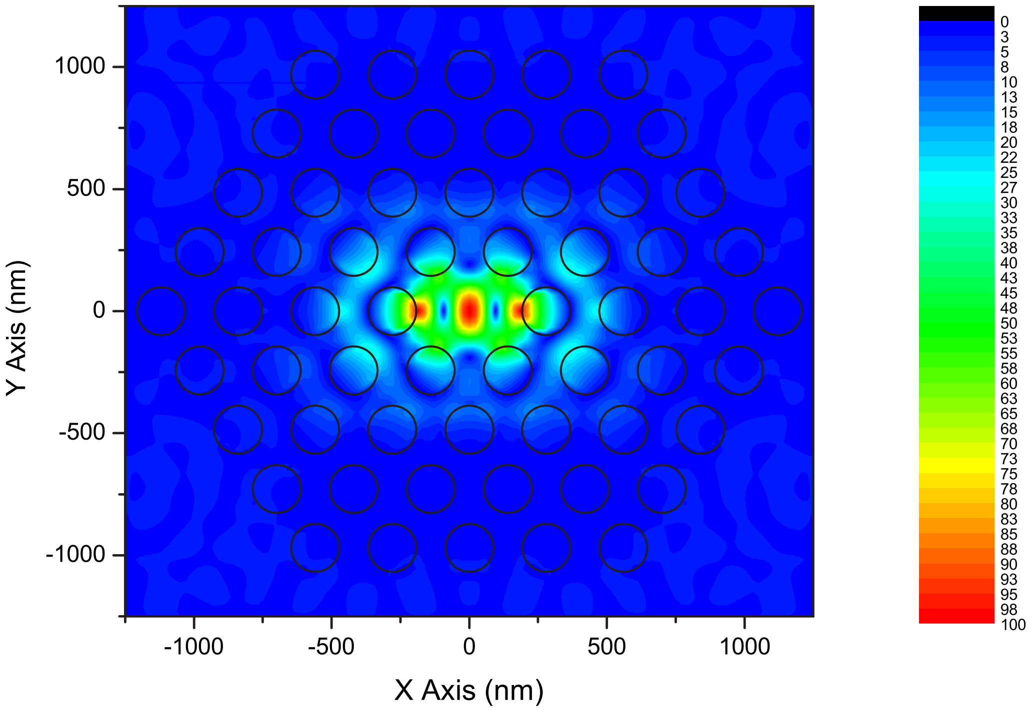

FIG. 5. (Color online) 3D-FIT calculated electric field modulus in the middle of the slab for the unperturbed microcavity with slab thickness $d=180$ nm.

In order to calculate the Purcell factor F_P, we first estimate the Q factor ($Q=\lambda/\Delta\lambda$) by a Lorentzian fit of the wavelength response of the cavity, obtaining the values of $Q=66$, $Q=80.2$, and $Q=154$ for the $d=180$ nm, $d=360$ nm, and $d=540$ nm cases, respectively. It has to be pointed out that theoretical Q factors depend on the number of hole layers of the microcavity. In this example, we have used only four layers, resulting in a small value of Q. Nevertheless, we will focus our attention only on the relative improvement of the optimized and nonoptimized cavity performances instead of on their specific behavior. The calculation of V has been made by transforming Eq. (2) in a sum over all the grid points of a 3D space containing the slab and keeping outside the excitation dipoles to avoid undesired artifact field peaks: x, $y \in$ [−900 nm, 900 nm] and $z \in$ [−100 nm, $d+100$ nm] with a space discretization step of $\Delta x=\Delta y=\Delta z=15$ nm (it has been proved that a reduction of the discretization step has no significant change on V). As a result, we obtain mode volumes of 0.3591, 0.6345, and 1.009 in $(\lambda/n)^3$ units for the $d=180$ nm, $d=360$ nm, and $d=540$ nm cases, respectively. Finally, using Eq. (1), we find that the unperturbed microcavities studied in this section have $F_P=14$, $F_P=9.6$, and $F_P=11.6$ for the three slab thicknesses, respectively. These values are in good agreement with the ones reported for similar structures.[18,27] As an example, in Fig. 5 we present the 3D-FIT calculated electric field modulus at the middle of the slab for the $d=180$ nm case.

IV. INVERSE DESIGN

Most of the strategies in the design of PC devices are based on the use of trial and error guided by knowledge and intuition. This is called direct design. However, from an implementation point of view, trial and error is inefficient and costly, providing little information about the quality of the solution. Only in the past few years has this problem been addressed by the use of a number of stochastic optimization algorithms. Such algorithms use a pool of solutions and guide their way using comparison. In that case, the physical intuition is used to limit the search space by setting up constraints. Stochastic algorithms are useful when we attempt to obtain the maxima of complicated functions of a large number of variables where it is impossible to study all configurations within reasonable times.

Our present objective is to generate the optimal geometrical arrangement of scattering elements that achieves a predefined performance. This type of problem is denoted as an inverse problem. In contrast to the direct problem, where a physical property is the result of the geometry of the structure considered, in the inverse problem the optimized geometry is a result of the physical property targeted. Nevertheless, to apply the inverse design it is necessary to solve the direct problem. In order to use the optimization algorithms used in the inverse design, we must first define a fitness function. The fitness function is simply a mathematical expression that quantifies the desired physical property(s) of the system that we want to optimize and its value is obtained by solving the direct problem. If we are interested in increasing the Purcell factor of the 3D unperturbed microcavities studied in the preceding section by reducing its mode volume, our fitness function will be simply the y component of the electric field in the center of the microcavity calculated with 2D-MST.

As mentioned earlier, the modification of the unperturbed microcavity will be accomplished by a rearrangement on the lattice positions of the scattering centers of an initially periodic array of cylindrical holes made in an infinitely thick slab of GaAs. We take advantage [see Eq. (2)] of the mirror symmetry of the sources with respect to the y axis and the double mirror symmetry of the microcavity with respect to the x and y axes to reduce the space search size. Notice that such characteristics give double mirror symmetry character to the mode studied in Sec. III with respect to the x and y axes. Any displacement made over a hole with coordinates x_0 and y_0 with $x_0 \geqslant 0$ and $y_0 \geqslant 0$ has its mirror symmetry equivalent displacement for the three remaining holes with coordinates $(-x_0, y_0)$, $(x_0, -y_0)$, and $(-x_0, -y_0)$; hence, the double mirror symmetry of the mode is maintained. So, although the microcavity has 60 scattering elements, the algorithm-guided position modifications will be done only over the 18 ones situated in the first quadrant, letting the remaining ones move according to their respective mirror symmetry counterparts. If the mode symmetry is maintained, the electric field peak y component will remain located at the center of the microcavity and will continue being the only nonzero one at this point. Consequently, a direct comparison with the unperturbed microcavity can be made. Once we have used intuition to reduce the search space and, at the same time, maintain the double mirror symmetry of the mode, it is necessary to specify how the holes are moved. We have chosen a displacement along the line defined by the origin of coordinates and the center of each hole. With that restriction, the relative position of each hole with respect to the equilibrium position is defined with a real number reducing even further the search space size. This real number is defined positive if the hole is moved away from the center of the microcavity or negative if is moved toward it. Therefore, we can relate the equilibrium position coordinates x_0 and y_0 of a generic hole with the perturbed ones x and y by the following equations:

$$x = x_0 + Tj \cos\left[\arctan\left(\frac{y_0}{x_0}\right)\right],$$

$$y = y_0 + Tj \sin\left[\arctan\left(\frac{y_0}{x_0}\right)\right], \tag{17}$$

where j is an integer that takes values between $j=-7$ and $j=7$ and T is a control parameter measured in nanometers called *temperature*. Its meaning will be explained later in Sec. IV B, where the simulated annealing optimization procedure is described.

Once we have set the parameters of the optimization problem, we can calculate the search space size, in other words, the number of possible configurations of the system. For each hole, there are 15 different positions. Considering that we have 18 holes in the first quadrant, for a fixed temperature, we obtain $15^{18} \cong 1.4 \times 10^{21}$ possibilities. Even using symmetry considerations to reduce the space search size, such a huge number makes a stochastic algorithm indispensable in tackling the optimization problem. Of course, the number of possibilities could be drastically reduced by, for example, letting j run from -2 to 2. Nevertheless, the quality of the optimized solution is directly related to the space search size. Again, we have selected these parameters considering our computing capabilities.

The drawback when a stochastic algorithm is used is that there is no guarantee that the global optimum has been found after the search is completed. In any case, what can certainly be assumed is that the solution obtained is among the best and has comparable quality to the global maximum. In the next sections, three different stochastic algorithms will be used: GA, SA, and a combination of both, namely, GA-SA. Therefore, in order to have an insight on each one's performance and be able to compare them, six different runs will be carried out on each case. The comparison and the results shown will be made between the best of the six runs for each algorithm.

A. Genetic algorithm

The GA belongs to a family of stochastic search algorithms called evolutionary computation, which are commonly used to solve a wide variety of engineering problems, and recently it has been applied in the field of photonic and phononic crystals.[23,24] This assemblage of algorithms is related to the optimization process used by nature itself: evolution. Like evolution, GA adapts individuals to a given environment and is by very simple means able to tackle very complex optimization problems. The evolution is guided through generations by mixing different individuals' chromosomes and new individuals with new modified characteristics are born, possessing some properties from parents. Those individuals who adapt better to the environment have the best chance of survival and hence give birth to more offspring creating a new generation more fit for survival than the previous one. Evolutionary computation tries to mimic the steps taken by nature and uses it as an optimization process. GA uses a population of individuals to guide the search. The concept of individual is employed to address a specific design in the optimization process. Therefore, the population of individuals is a group of designs. For the specific problem considered here, each individual corresponds to a fixed distribution of holes in the XY plane. In GA optimization, the individual is normally described as a string of binary bits called a chromosome and how chromosomes are associated to each structure is called codification. The chromosome is divided up into genes, where each gene is related to one specific hole. Therefore, if each hole can be placed on 15 positions, its gene can be represented with a binary string of length 4 that has $2^4 = 16$ combinations. Notice that since the number of positions is odd, it is impossible to find a binary string with the same number of possible combinations (for a binary string of length N, there are 2^N combinations). To solve this problem, we link two different genes to the equilibrium position. This will have no effect on the optimization results since this only slightly increases the search space. Finally, each individual is represented with a chromosome with a string of 18 genes and a length of $18 \times 4 = 72$ bits. A possibility would be to choose the simplest codification possible as in Ref. 23. In this work, the length of the genes is limited to one single bit, coding the presence or the absence

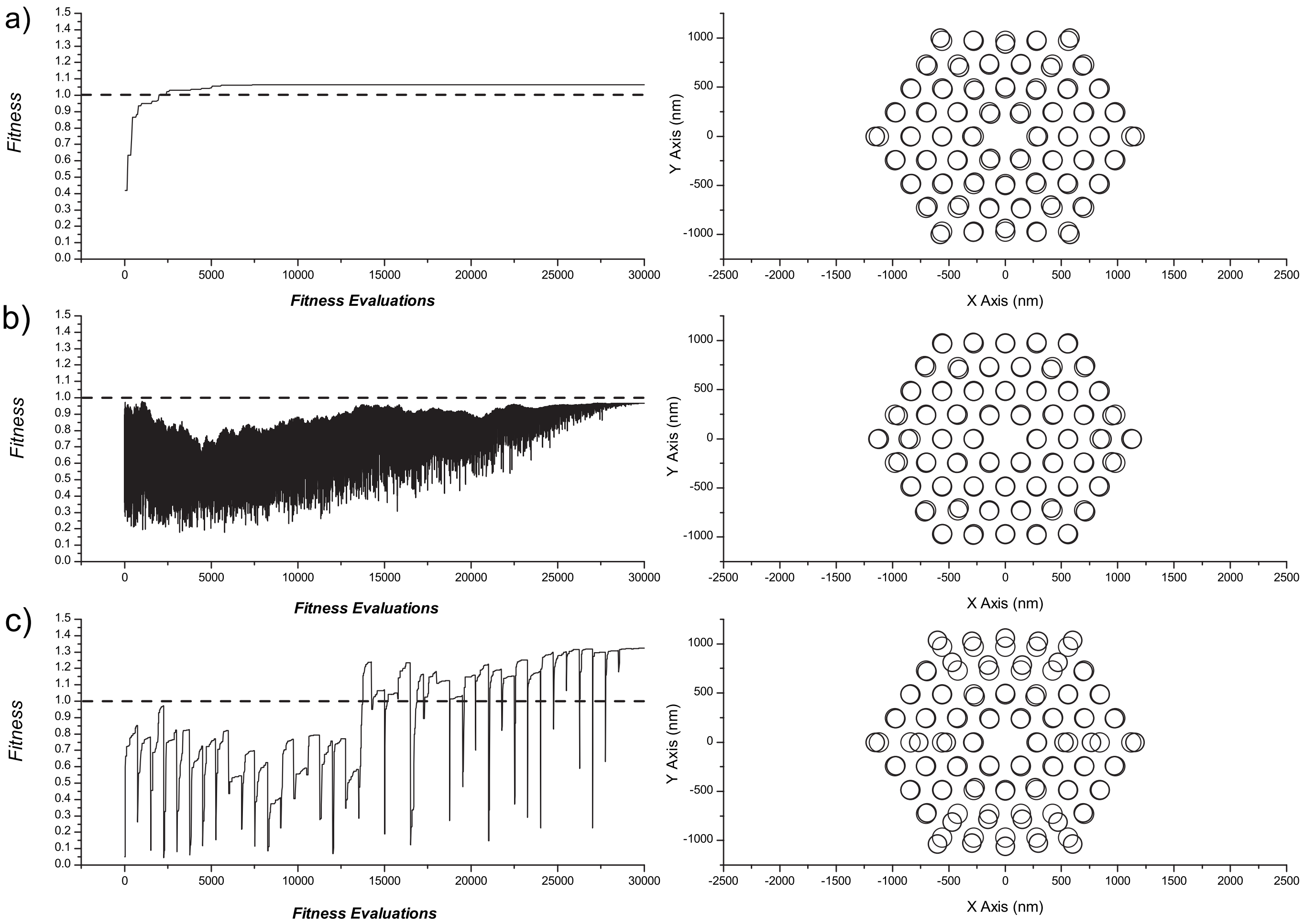

FIG. 6. (a) (Left) GA evolution of the fitness function of the best individual of the population vs number of times that the fitness function is calculated. The dashed straight line represents the fitness function of the unperturbed structure. (Right) Schematic representation of the structure obtained (thick circles) and of the unperturbed periodic structure (thin circles). (b) The same as (a) but with the SA algorithm. (c) The same as (a) but with the GA-SA combined algorithm. In this case, a strongly aperiodic structure is found.

of a cylinder at a fixed lattice site. Nevertheless, the aim of this work is to construct an efficient resonant cavity so the elimination of any cylinder would lead to a leaky structure.

At that point, to be able to apply GA, each individual needs to be given a value corresponding to how well this individual solves the problem. This is the fitness function that in our case is the y component of the electric field on the center of the microcavity. GA mimics the evolutionary process of a population by identifying three different operations, natural selection, the mating act, and genetic mutation which are called operators *selection*, *crossover*, and *mutation*. First, an initial population of individuals is set randomly to exclude any external guidance. The first operator applied to the population is selection. Selection culls the population selecting better solutions over worse by using a survival of the fittest approach. The second operator is crossover that directs the mating act. This operator takes two chromosomes as input, given by selection, and mixes these two strings to produce a new individual with properties from the two parents. Before the new individual is added to the new population, it is modified by the mutation operator. Mutation simply introduces some randomness into the solution, normally with some low probability, in order to avoid convergence to a local maximum. These three operators are repeatedly applied until the new population has reached the size of the initial one. The old population is then replaced by the new one, with the exception of the best fitted solution, which automatically is copied into the new population. This practice is called *elitism*. This process is repeated until convergence and the optimal solution is found to be the best one of the population.

Figure 6(a) (left) shows the evolution of the best value of the population normalized component with respect to the nonperturbed microcavity as a function of the number of times that the fitness function is calculated. The result displayed corresponds to the best run among six optimizations. As can be seen, the algorithm rapidly converges around 10 000 fitness function evaluations with a value of 1.064. This means that the rearrangement of the scattering centers has led to an increase of 6.4% in the E_y component at the center of the microcavity with respect to the original structure. Such rearrangement can be seen graphically on the right side of Fig. 6(a), where the unperturbed periodic structure for comparison purposes is also presented. In this calculation, a population size of 50 individuals has been employed, an unchanging temperature of 5 nm and a mutation probability of 0.01 have been considered, and the evolutionary process has been stopped at generation 600. For details about the meaning of the optimization parameters, the reader can consult Ref. 21. It has to be pointed out that MST formalism is only valid if the cylindrical inclusions do not touch. In order to avoid overlap between adjacent holes, the algorithm gives automatically a null value to the fitness of the individuals which have one or more holes overlapped. The algorithm tends to wipe out those individuals, leaving only structures in which the MST calculation can be considered accurate. Although demonstrating fast convergence, because of the modest increment in the y electric field component compared to the unperturbed microcavity, we can conclude that GA procedure has been proved unsuited to this optimization problem. The reason for this is that the holes are confined around initial equilibrium positions (periodic array of the unperturbed structure). With the aim of overcoming this constraint, a different stochastic algorithm is introduced.

B. Simulated annealing

This general optimization method was first introduced by Kirkpatrick *et al.*[22] It simulates the softening process (annealing) of metal. The metal is heated up to a temperature near its melting point and then slowly cooled down. This permits the particles to move toward a uniform crystalline structure with an optimum energy state. SA is a variation of the hill-climbing algorithm. The difference between SA and the hill-climbing algorithm is that if the fitness of a new trial solution (E_{i+1}) is less than the fitness of the current solution (E_i), in SA the trial solution is not automatically rejected, as it is in the hill-climbing algorithm. This trial solution becomes the current solution with a certain transition probability p which depends on the difference in fitness $\Delta E = E_{i+1} - E_i$ and the temperature T. The acceptance of bad transitions tries to avoid getting stuck in a local maximum. Temperature is an abstract control parameter that here represents the degree of similitude with respect to the equilibrium position of the holes [see Eq. (17)]. The transition probability for a given temperature and a given difference in fitness is

$$p = \begin{cases} 1 & \text{if } E_{i+1} > E_i \\ e^{\Delta E/T} & \text{if } E_{i+1} < E_i. \end{cases} \tag{18}$$

The algorithm starts with the equilibrium state of the unperturbed microcavity and a starting temperature T_0. This state has fitness $E_0 = 1$ corresponding to the normalized y component of the electric field in the center of the cavity. Then, a random structure is generated whose hole positions are defined by Eq. (17) and its fitness E_1 is calculated. This state, according to Eq. (18), has probability p to become the new equilibrium state. This annealing step process is repeated until the temperature takes a null value. The way the temperature decreases along the cooling process is called the *cooling schedule* which governs how likely a bad transition is accepted as a function of time. In the beginning of the search, we are interested in using randomness to explore the search space widely, so the probability of accepting a negative transition is high. As the search progresses, we seek to limit transitions to local improvements and optimizations so the probability of moving from a high-fitness state to a lower-fitness state is reduced. The cooling schedule is determined by the initial temperature T_0 and the temperature decrement function. Several decrement functions can be chosen but a detailed study of this subject is beyond the scope of this work. We have selected the simplest one that seems to work properly[28] where the temperature is reduced linearly according to the formula

$$T_i = T_0 - \frac{iT_0}{N}, \tag{19}$$

where T_i is the temperature of the annealing step i, and N is the number of annealing steps ($i=0,\ldots,N$). In the optimization example shown in left side of Fig. 6(b), which corresponds to the best result among six runs, one can see the evolution of the fitness function as a function of the number of times that is calculated. We have used an initial temperature of 0.1 nm and 30 000 annealing steps. The choice of a higher initial temperature has the consequence of a fast convergence to zero of the fitness function due to overlapping of the cylinders. Note that the fitness function has been calculated the same number of times as in the GA case (population 50 individuals × 600 generations) for comparison purposes between the optimization methods. The right side of Fig. 6(b) illustrates the resulting structure superposed with the initial unperturbed periodic structure. As it is manifest, there is no improvement with respect to the periodic structure as the fitness function is less than 1. The difference with the preceding case is that whereas the initial state structure is always the same in GA (the periodic unperturbed microcavity), in SA this state is permitted to change with some probability while the optimization is running. This means that in the GA case the positions of the holes are constrained to move around fixed points, while in the SA case the holes can migrate freely. Surprisingly, although the holes have the possibility to be positioned far away from their initial periodic positions, the resultant structure almost maintains its periodic original nature. Therefore, the SA method is not suitable if we intend to optimize a periodic structure by breaking its periodic pattern. The spontaneous emergence of periodic patterns in a biological inspired simulation of photonic structures has been recently reported.[29]

C. Combined GA-SA algorithm

At this point, the optimization of a 2D microcavity using two different stochastic algorithms has been studied. On one hand, the GA optimization, although with fast convergence, leads to a structure whose scattering centers are located around the equilibrium positions of the unperturbed microcavity because of a geometrical constraint. On the other hand, with the SA algorithm, an almost periodic structure with worse performance is also obtained due to the nature of the algorithm. While in the GA case the holes do not have the possibility to migrate freely from their original periodic positions, the SA case is not suitable in order to improve the performance of a periodic microcavity by breaking their periodicity. In this section, we describe a combined GA-SA algorithm that gathers the advantages of both methods while their drawbacks are eliminated. As previously shown, in the

SA method each repositioning is made randomly and the acceptance of each new configuration depends on a probability. In the combined GA-SA algorithm, instead of generating randomly the new state, it is generated by a GA run. Thus, this algorithm is a sequence of GA runs in which the acceptance of a transition to an initial GA state is determined by the same probability as in the SA case. In addition, the temperature is gradually decreased in each GA run. We have made a sequence of 40 annealing steps (GA runs) with an initial temperature of 5 nm. Each GA run has a population size of 15 individuals which evolve over 50 generations and with mutation probability of 0.01. Figure 6(c) (left) describes the evolution of the best value of the fitness function of the population as a function of the number of times that it is calculated. The example shown is the best among six runs of the GA-SA combined algorithm. Figure 6(c) (right) shows the resulting structure and the unperturbed one for comparison purposes. At the end of the optimization process, a structure with fitness function of 1.323 has been found. This means an increment of the E_y component of 32.3% with respect to the unperturbed microcavity. The structure obtained is rather different from the original periodic one as the holes can move freely over the plane. At this point, it must be kept in mind that although the structure is different, it has the same resonant wavelength of 1143.8 nm as the original one since this is the wavelength at which it has been optimized (see Sec. III).

Figure 7(a) illustrates the comparison between the mode profiles of the unperturbed microcavity and of the GA-SA optimized one. These profiles are calculated in 2D with the MST method along the x axis. An increment of E_y component of the optimized structure from 1 to 1.323 at the central peak with respect to the periodic unperturbed one has been found. This increment is also recognizable in Fig. 6(c) after 30 000 fitness evaluations. Nevertheless, once we have found a 2D-optimized structure, it is necessary to consider the behavior of its 3D optimized counterparts to examine to what extent E_y has been increased, and as a consequence, the mode volume has been reduced. In Figs. 7(b)–7(d), the same mode profiles as in Fig. 7(a) are shown, now calculated with the 3D-FIT method in the middle of the slab for the $d=180$ nm, $d=360$ nm, and $d=540$ nm cases, respectively. The effect that the optimization procedure made on the 2D structure has over its 3D counterparts is remarkable, where the main central peak and the lateral peaks of the mode have been increased. Also, Figs. 7(b)–7(d) show that the effect of the optimization is more noticeable when the thickness of the slab is augmented. This is a logical consequence since the optimization has been done on a 2D structure. This fact demonstrates our assumption that the optimization made in 2D structure has a direct consequence on its 3D optimized equivalent.

It has to be pointed out that the resonant wavelengths of the unperturbed and of the modified microcavities are slightly different. As it was shown in Sec. III, the original periodic structure has a resonant wavelength of 968 nm, while the optimized one has 971 nm. Similar small shifts in wavelength have been detected in the $d=360$ nm and $d=540$ nm cases. Figures 7(b)–7(d) give us an indication that the mode volume has been effectively reduced; nevertheless, to make sure that this reduction has been achieved, it is necessary to calculate the electric field over the whole space in order to apply Eq. (2). Following the same method as in Sec. III, with the same FIT and mode volume calculation parameters, we obtain mode volumes of 0.3581, 0.5840, and 0.7993 in $(\lambda/n)^3$ units for the cases $d=180$ nm, $d=360$ nm, and $d=540$ nm, respectively. Comparing with the value obtained for the unperturbed microcavities of 0.3591, 0.6345, and 1.0089, or what is the same, 0.3%, 8%, and 20.8% mode volume reduction, we can assert that the combined GA-SA algorithm is a useful tool in our objective of reducing the mode volume of a 3D structure when applied to its 2D equivalent as long as we deal with a quasi-two-dimensional structure. However, the Purcell factor F_P depends as much on mode volume as it does on the quality factor Q of the microcavity [Eq. (1)]. Therefore, it is essential to calculate Q and see how it has been affected by the optimization focused on the mode volume reduction. Consequently, we calculate the Q by a Lorentzian fit to the wavelength response of the cavity ($Q=\lambda/\Delta\lambda$), obtaining values of $Q=82.7$, $Q=139$, and $Q=470$ for the three different thicknesses. Thus, keeping in mind that the unperturbed microcavities have Q values of 66, 80.2, and 154, we can conclude that the mode volume oriented optimization does not have the effect of a reduction in Q; moreover, it increases with the thickness of the slab. Fi-

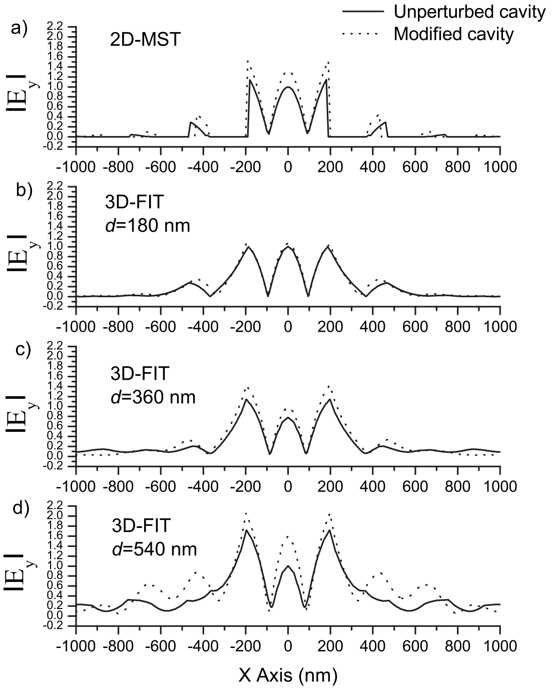

FIG. 7. (a) Normalized mode profile comparison along the x axis of the resonant mode calculated with the 2D-MST method for the unperturbed microcavity (continuous line) and for the GA-SA modified microcavity (dotted line). In the zones where holes are located, the value of the field has been set to zero. The resonant wavelength in both cases is 1143.8 nm. [(b), (c), and (d))] The same as (a) but this time calculated with the 3D-FIT method, in the middle of the slab, with the thickness of the slab $d=180$ nm, $d=360$ nm, and $d=540$ nm, respectively. It can be observed that the optimization is more effective when the thickness of the slab is larger.

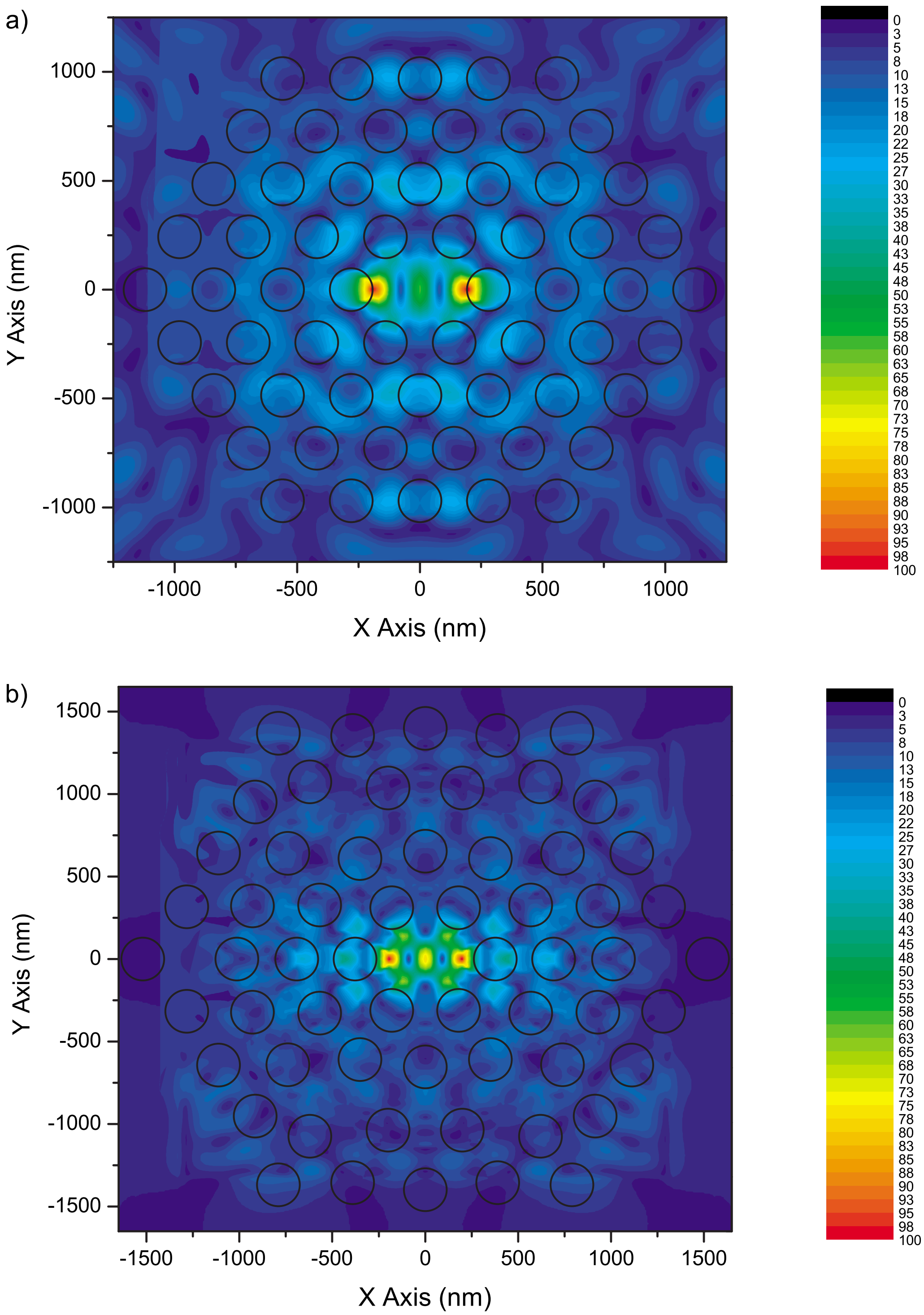

FIG. 8. (Color online) 3D-FIT calculated electric field modulus in the middle of the slab for the (a) unperturbed cavity and (b) GA-SA optimized microcavity. The thickness of the slab is $d=540$ nm.

nally, using Eq. (1), we find that the GA-SA optimized microcavities have Purcell factors $F_p=17.5$, 18.1, and 44, or what is the same, 25%, 88.5%, and 279% Purcell factor enhancement. To notice the mode volume reduction in Fig. 8 we present the 3D-FIT calculated electric field modulus in the middle of the slab for the $d=540$ nm case of the (a) unperturbed and (b) optimized microcavities. In summary, the GA-SA optimization works properly if the photonic crystal microcavity has been made on a thick enough slab that can be considered as quasi-two-dimensional. This procedure may be useful when we deal with cavities where the thickness of the slab is large as, for example, in vertical-cavity surface-emitting lasers.[30] Nevertheless, here we are concerned in microcavities where the slab thickness must be as thin as possible because in this way the maximum electric field peak is located in the geometrical center of the cavity [see Fig. 4(b), $d=180$ nm case] and it has the smallest mode volume. In the next section, we introduce a different technique that is able to reduce the mode volume of a PC microcavity made on a thin slab.

V. OPTIMIZED MICROCAVITY WITH HIGH-INDEX INCLUSIONS

A. Optimization

In the preceding section, we have developed an optimization method able to reduce the mode volume of a periodic PC microcavity by making an adequate redistribution of the scattering centers. In this section, we introduce high-refractive-index scattering elements in the center of the microcavity with the purpose of finding an even greater reduction in the mode volume. These high-index elements will cause an enhancement of the electric field in the region in between them. In contrast to previous work[19] where the high field region was in air, this region will be situated in the bulk GaAs semiconductor where a quantum dot can be grown. As high-index scattering elements, we have used two small cylinders of radius 25 nm located at $x=0$, $y=27.5$ and $x=0$, $y=-27.5$ where the coordinates are expressed in nanometers. With this configuration, we find the y electric field component of the y-dipole mode perpendicular to the high-index cylinder interfaces and in the geometrical center of the microcavity.

For the numerical calculations, the dielectric constant of the high-index inclusions has been chosen to be 25, greater than that of GaAs, 12.6. With these geometric specifications, we are ready to apply the combined GA-SA algorithm. In a first run, we found that the y electric component rapidly diverges to very high values due to the fact that the algorithm tends to bring the high-index cylinders together. This is an expected behavior since the electric field amplitude enhancement in the low-index region is increased as the gap width between interfaces decreases.[19] The aim of this paper is to design a microcavity where a quantum dot could be located between the two high-index elements. Thus, we fix them at original locations, $x=0$, $y=27.5$ and $x=0$, $y=-27.5$, with a resulting gap width of 5 nm, and disallow their movement. Although this allows for only a small quantum dot, we are using this as a starting design which can be further modified to allow for more realistic quantum dot dimensions. Once the positions of the small cylinders have been fixed, we apply our GA-SA algorithm to the remaining cylinders to find the optimized distribution of holes that maximizes the y electric field component, and thus, as it has been shown, to obtain a small mode volume microcavity.

Figure 9(a) shows the fitness evolution of the best individual of the population as a function of the amount of fitness evaluations. As in Fig. 6 (left), the value of the y electric field component at the origin of coordinates (fitness function) is normalized with respect to the value obtained for the unperturbed periodic microcavity studied in Sec. III. We have employed the same parameters as in Sec. IV C concerning population size, initial temperature, mutation probability, number of generations, and annealing steps. Notice that as subwavelength size peculiarities of the field are expected, it is necessary to take into account a large amount of terms of the Bessel expansion $(2l_{\max}+1)$ in order to describe accurately these features [see Eq. (16)]. Nevertheless, a full run with the maximum value of $l_{\max}$ achievable to support subroutine stability ($l_{\max}=9$) is prohibitive in terms of calculation time. To overcome this situation, we have performed a first run taking $l_{\max}=3$ with 30 000 fitness calculations. Then, we have incremented $l_{\max}$ until 6 and we have made a short transition run of three annealing steps taking as original structure the one obtained with the first run. Finally, we made the last run with $l_{\max}=9$ and 5 annealing steps being the

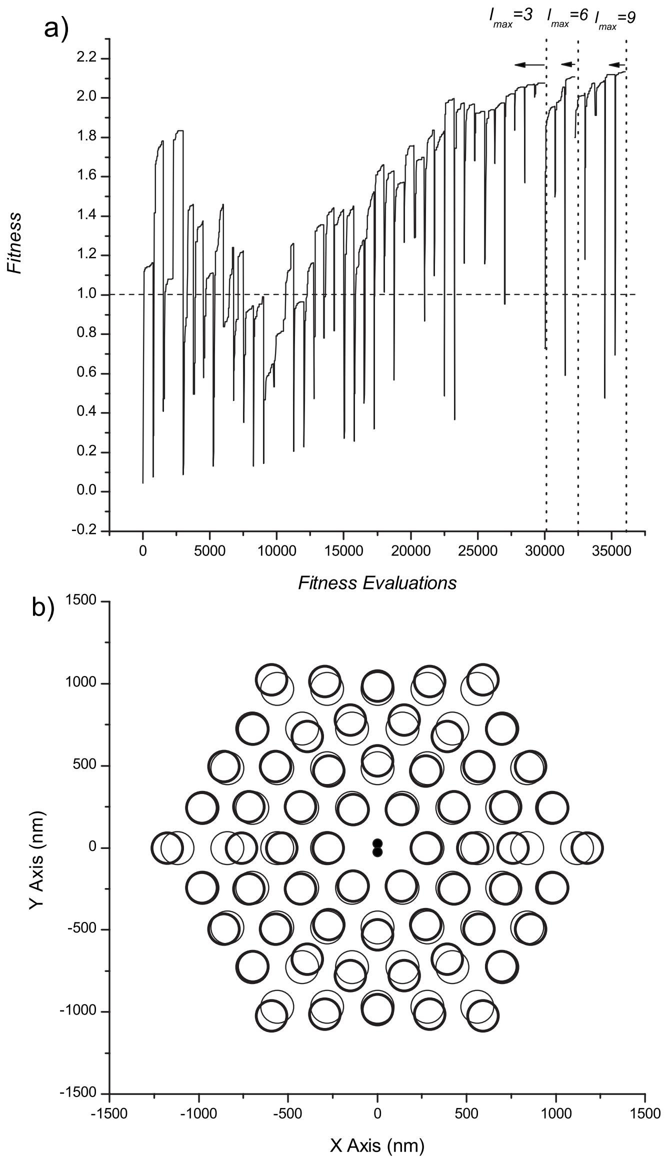

FIG. 9. (a) GA-SA evolution of the fitness function of the best individual of the population vs number of times that the fitness function is calculated. The dashed straight line represents the fitness function of the unperturbed structure without high-index inclusions. The dotted vertical lines delimit the three different runs that form the optimization with $l_{\max}$ taking values 3, 6, and 9. (b) Schematic representation of the structure obtained (thick circles) and of the unperturbed periodic structure (thin circles). The two high-index cylinders are presented in the center of the cavity.

initial temperature of the three runs 5, 1, and 1 nm, respectively. Thus, we ensure accuracy in the solution without the necessity of carrying out the whole optimization run with a large value of $l_{\max}$. The three runs are delimited by vertical dotted lines in Fig. 9(a). As before, in the optimization process we have used a wavelength of 1143.8 nm corresponding to the resonant state calculated for the unperturbed structure using 2D-MST with $l_{\max}=3$. As a result, we obtain a 2D microcavity where the y electric field component at the center is 2.1327 times higher than that of the unperturbed 2D periodic structure with no high-index inclusions. Figure 9(b) illustrates the hole distribution of both of these structures.

B. 3D-FIT analysis

Once we have obtained the 2D-optimized microcavity with high-index cylindrical inclusions with the GA-SA algorithm, it is necessary to study its 3D counterpart with the FIT method in a manner similar to those followed in the preceding sections. We have chosen in this case the thickness of the slab to be 180 nm and we use the same 3D-FIT parameters as before, taking special care in increasing the grid line density along the x and y axes with a space discretization step of 1 nm in the center of the cavity to take account of the subwavelength sized fine details of the field. The first step is to find the resonant wavelength and Q factor by fitting the Fourier transformed temporal response of the cavity to a Lorentzian curve. A value of 981 nm has been obtained. Therefore, we find that the resonant wavelength at which the optimization has been carried out (1143.8 nm) is redshifted around 163 nm with respect to the resonant wavelength obtained for the 3D equivalent microcavity. Besides, a value of 86 for the quality factor Q has been obtained. It is important to check whether the high electric field enhancement with respect to the original 2D microcavity, obtained with the inclusion of high-index cylinders and the optimization procedure, is reflected in the mode volume reduction of the 3D equivalent microcavity. Let us focus on the $d=180$ nm case since it has the smallest mode volume and because it is the kind of microcavity with dimensions more widely analyzed by most authors. We have reduced the discretization step on the calculation of the mode volume in order to increase accuracy due to the fine details of the field existent between the high-index inclusions. This time, we have utilized a space discretization step of 5 nm instead of 15 nm as before. As in Secs. III and IV C, we calculate the mode volume and we obtain a value of 0.086 91 in $(\lambda/n)^3$ units. Such an extremely small mode volume can be visualized in Fig. 10, where the profile of $|E_y|$ is presented along the x axis in the middle of the slab. Also, the profile of the field for the unperturbed microcavity without high-index inclusions has been presented for comparison purposes. It also must be pointed out that with this procedure, it is possible to overcome the diffraction limit of a cubic half wavelength $(\lambda/2n)^3=0.125(\lambda/n)^3$. Finally, by using Eq. (1), we obtain a huge Purcell factor $F_P=75$. Keeping in mind that the Purcell factor of the unperturbed microcavity ($d=180$ nm case) was 14, we found a 536% increment in the GA-SA optimized microcavity with high-index inclusions. In order to distinguish between the effect caused by the optimization and the inclusion of high-index elements, we have also calculated the mode volume reduction correspondent with the unperturbed periodic microcavity with high-index inclusions. As a result of this calculation, we found its mode volume to be 0.1012. Comparing with the result obtained with the simultaneous use of both techniques (0.086 91) we can affirm that the optimization has in this case a secondary role being the dominant effect caused by the high-index inclusions.

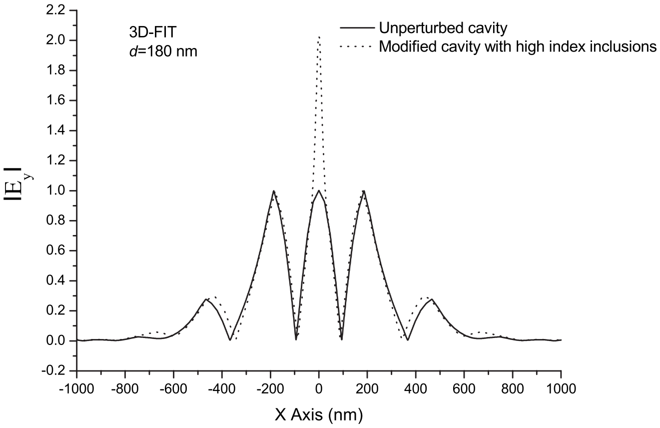

FIG. 10. Mode profiles along the x axis in the middle of the slab of the 3D optimized microcavity with high-index inclusions (dotted line) and unperturbed microcavity (continuous line) for the $d=180$ nm case. The mode profile is represented by the y component of the electric field.

According to referenced previous work,[19] the ratio between the mode volume before and after introducing the subwavelength discontinuity, and therefore the Purcell factor increase considering little change of Q, was reported to be approximately $(\varepsilon_H/\varepsilon_L)^{5/2}$, where L and H denote low and high dielectric constant. In our case, we have used $\varepsilon_L=12.6$ corresponding to GaAs and $\varepsilon_H=25$ which leads, following this equation, to an enhancement factor of 5.545 times the Purcell factor of the unperturbed microcavity. Besides, by the use of different procedures, we have found this factor to be 5.36. The effect of the mode volume reduction can be appreciated in Fig. 11, where the 3D-FIT calculated electric field modulus in the middle of the slab for the optimized microcavity with high-index inclusions is presented.

For the high-index cylinders, we have used a dielectric constant of 25 without referring to any particular material, simply to fulfill the requisite of being higher than that of the substrate. Some different materials could be chosen instead in order to take advantage of that mode volume reduction effect provided the two following conditions are met. First, a quantum dot must be able to be grown in the substrate. Second, the inclusions must have a higher dielectric constant with respect to the slab, and moreover the higher the difference between both, the better. Therefore, for example, similar microcavities can be created using slabs of gallium nitride ($n_{\mathrm{GaN}}=2.33$), where an InGaN quantum dot can be grown, and high-index cylinders of silicon ($n_{\mathrm{Si}}=3.54$). With these materials, we have $(\varepsilon_H/\varepsilon_L)^{5/2}=8.12$; therefore, we expect to find similar Purcell factor enhancements. We have done

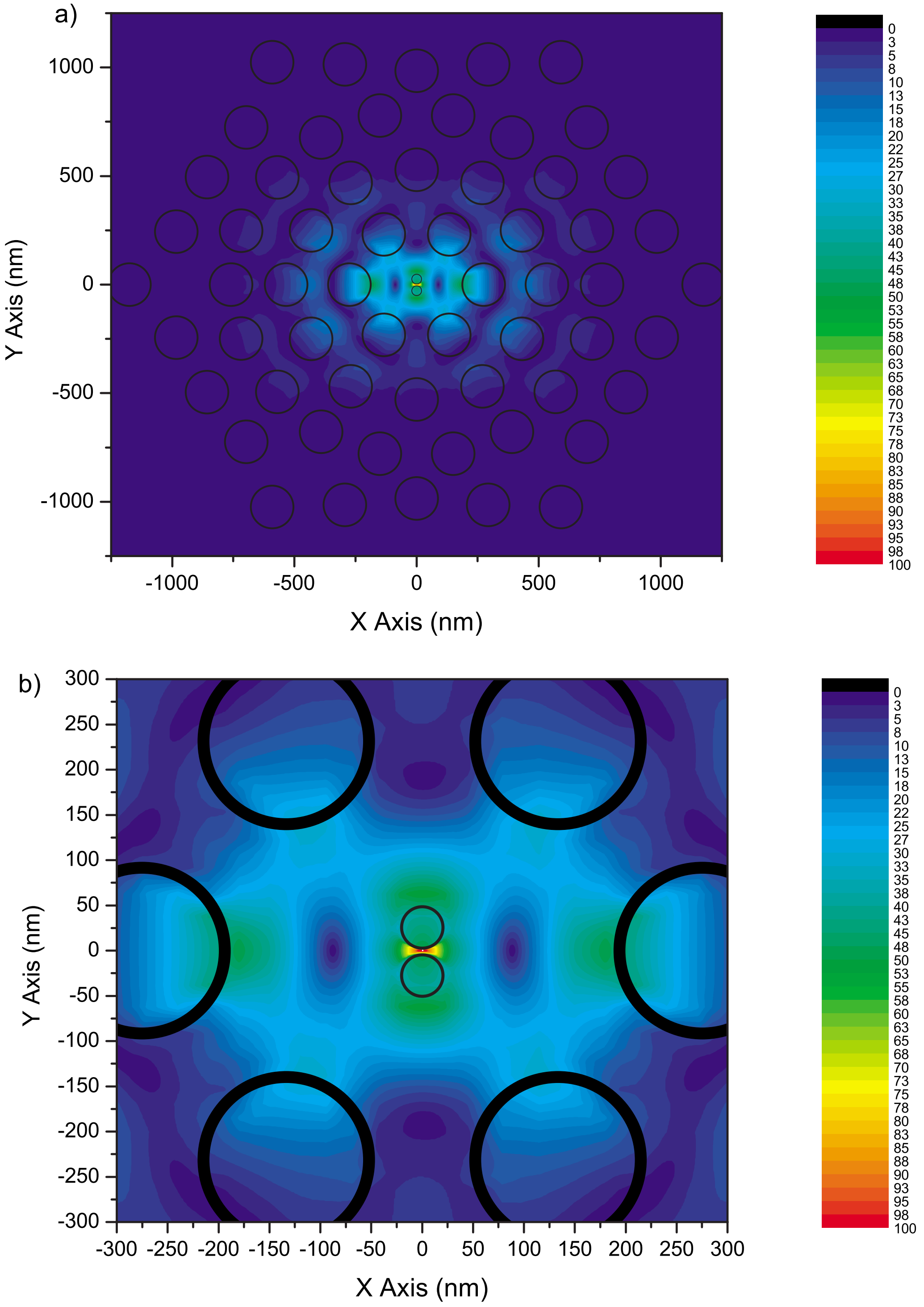

FIG. 11. (Color online) (a) 3D-FIT calculated electric field modulus in the middle of the slab for the GA-SA optimized microcavity with high-index inclusions. (b) The fine details of the field between the high-index cylinders. The thickness of the slab is $d=180$ nm.

calculations using this time GaN and Si as constituent materials of the substrate and the high-index inclusions. First, for the original unperturbed microcavity without high-index cylinders, we have found values of 57, 0.4231, and 10.23 for Q, V, and F_P, respectively, with resonant wavelength of 672 nm. Secondly, we have studied the same microcavity but now with the high-index inclusions obtaining values of 40, 0.0673, and 45.2 for Q, V, and F_P with resonant wavelength of 687 nm. This means a mode volume reduction of 628% and a Purcell factor enhancement of 441% caused by the inclusion of Si cylinders in the GaN periodic microcavity. Several factors should be taken into account in future works concerning the practical implementation of the microcavities studied in this paper. In our opinion, the main concern must be focused on finding materials to fulfill any particular needs and with the feasibility of being manufactured.

VI. CONCLUSIONS

In conclusion, we have theoretically analyzed and modified a photonic crystal slab microcavity in order to obtain the smallest mode volume possible and consequently with maximized Purcell factor. We utilized two different theoretical approaches to describe the properties of the microcavities studied. First, multiple scattering theory has been used to deal with 2D structures. Some theoretical improvements have been addressed in order to speed up the calculations, as, for example, a relation between the elements of the scattering matrix. Secondly, we have used the FIT technique to evaluate the properties of the 3D structures. The properties of interest have been the quality factor and the mode volume of the microcavities considered although FIT has also been used to calculate mode profiles and snapshots. The parameters used throughout the paper have been chosen envisaging the possibility of using a quantum dot as an appropriate emitter to build single photon sources. Therefore, the microcavities proposed have a maximum electric field in the GaAs substrate, although the use of other materials is also possible. Three different stochastic optimization algorithms have been proposed to design the microcavities. The genetic algorithm and the simulated annealing algorithm have demonstrated not to be useful for the specific problem considered, whereas a combination of both has been proven to be efficient. A remarkable effect has been verified when employing the simulated annealing approach to optimize a periodic photonic crystal microcavity. In the same way that solids crystallize in periodic patterns, photonic crystals optimized with the simulated annealing method also crystallize in periodic patterns. Therefore, this method is not suitable if the PC microcavity is to be optimized by breaking its periodicity. It also has been demonstrated that the optimization made over a 2D structure has a direct consequence on its 3D counterpart although its resonant wavelength is blueshifted.

Finally, the inclusion of small high-index cylinders at the center of the microcavity has led to an extremely small mode volume optimized microcavity with an ultrahigh Purcell factor of 75. This value is double the one reported for the dipole mode in a similar PC microcavity.[27] This value has been achieved, thanks to the huge enhancement experienced by the electric field in the vicinity of the subwavelength discontinuities introduced. Thanks to the multiobjective character of the optimization procedure presented in this work, this method can also be used to optimize the Q factor at the same time as minimizing V.

ACKNOWLEDGMENT

The authors would like to acknowledge the financial support provided by the Spanish Ministry of Education and Science (Programa de becas postdoctorales de la Secretaría de Estado de Universidades e Investigación Ex 2005, Ref. 0533).

---

*lsanchis@fis.upv.es

[1] M. Lončar, A. Scherer, and Y. Qiu, Appl. Phys. Lett. **82**, 4648 (2003).

[2] O. Painter, R. K. Lee, A. Scherer, A. Yariv, J. D. O'Brien, P. D. Dapkus, and I. Kim, Science **284**, 1819 (1999).

[3] S. Noda, A. Chutinan, and M. Imada, Nature (London) **407**, 608 (2000).

[4] W.-H. Chang, W.-Y. Chen, H.-S. Chang, T.-P. Hsieh, J.-I. Chyi, and T.-M. Hsu, Phys. Rev. Lett. **96**, 117401 (2006).

[5] N. Gisin, G. Ribordy, W. Tittel, and H. Zbinden, Rev. Mod. Phys. **74**, 145 (2002).

[6] E. Knill, R. Laflamme, and G. J. Milburn, Nature (London) **409**, 46 (2001).

[7] Q. A. Turchette, C. J. Hood, W. Lange, H. Mabuchi, and H. J. Kimble, Phys. Rev. Lett. **75**, 4710 (1995).

[8] E. Waks and J. Vuckovic, Phys. Rev. Lett. **96**, 153601 (2006).

[9] A. Auffeves-Garnier, C. Simon, J.-M. Gerard, and J.-P. Poizat, arXiv:quant-ph/0610172 (unpublished).

[10] T. F. Krauss, R. M. D. L. Rue, and S. Brand, Nature (London) **383**, 699 (1996).

[11] S. G. Johnson, S. Fan, P. R. Villeneuve, J. D. Joannopoulos, and L. A. Kolodziejski, Phys. Rev. B **60**, 5751 (1999).

[12] K. Srinivasan and O. Painter, Opt. Express **10**, 670 (2002).

[13] J. Vučković, M. Lončar, H. Mabuchi, and A. Scherer, Phys. Rev. E **65**, 016608 (2001).

[14] C. Santori, D. Fattal, J. Vuckovic, G. S. Solomon, and Y. Yamamoto, Nature (London) **419**, 594 (2002).

[15] E. Burstein and C. Weisbuch, *Confined Electrons and Photons: New Physics and Applications* (Plenium, New York, 1994).

[16] D. Englund, I. Fushman, and J. Vuckovic, Opt. Express **13**, 5961 (2005).

[17] C. Kurtsiefer, S. Mayer, P. Zarda, and H. Weinfurter, Phys. Rev. Lett. **85**, 290 (2000).

[18] R. Coccioli, M. Boroditsky, K. W. Kim, Y. Rahmat-Samii, and E. Yablonovitch, IEE Proc.: Optoelectron. **145**, 391 (1998).

[19] J. T. Robinson, C. Manolatou, L. Chen, and M. Lipson, Phys. Rev. Lett. **95**, 143901 (2005).

[20] V. R. Almeida, Q. Xu, C. A. Barrios, and M. Lipson, Opt. Lett. **29**, 1209 (2004).

[21] D. E. Goldberg, *Genetic Algorithms in Search, Optimization and Learning* (Addison-Wesley, Reading, 1989).

[22] S. Kirkpatrick, C. D. Gelatt, and M. Vecchi, Science **220**, 671 (1983).

[23] L. Sanchis, A. Håkansson, D. López-Zanón, J. Bravo-Abad, and J. Sánchez-Dehesa, Appl. Phys. Lett. **84**, 4460 (2004).

[24] A. Håkansson, J. Sánchez-Dehesa, and L. Sanchis, Phys. Rev. B **70**, 214302 (2004).

[25] D. Felbacq, G. Tayeb, and D. Maystre, J. Opt. Soc. Am. A **11**, 2526 (1994).

[26] E. T. Wittaker and G. N. Watson, *A Course of Modern Analysis* (Cambridge University Press, Cambridge, United Kingdom, 1965).

[27] H. Y. Ryu and M. Notomi, Opt. Lett. **28**, 2390 (2003).

[28] S. Rees and R. C. Ball, J. Phys. A **20**, 1239 (1987).

[29] A. Gondarenko, S. Preble, J. Robinson, L. Chen, H. Lipson, and M. Lipson, Phys. Rev. Lett. **96**, 143904 (2006).

[30] P. S. Ivanov, M. Dragas, M. Cryan, and J. M. Rorison, J. Opt. Soc. Am. A **22**, 2270 (2005).

[31] www.cst.com